Research Article Vol. 34, No. 2 / 26 Jan 2026 / Optics Express 2770
Optics EXPRESS

Super-resolution structured illumination microscopy of cellular nanopores using near-infrared fluorescent probes

SYLVIA MARIE STEINECKER,[1,6] HENNING ORTKRASS,[1] MARCEL MÜLLER,[1] JASMIN CELINE SCHÜRSTEDT-SEHER,[1] SURJENDU BIKASH DUTTA,[1] ANGELA KRALEMANN-KÖHLER,[2] ANNIKA KIEL,[2] SÖNKE BAUMANN,[3] GERHARD HOLST,[4] JAN SCHULTE AM ESCH,[2,5] AND THOMAS HUSER[1,7]

[1]*Biomolecular Photonics Research Group, Faculty of Physics, Bielefeld University, Bielefeld, Germany*
[2]*Department of General and Visceral Surgery, Liver and Tumor Biology, Medical Faculty OWL, Bielefeld University, Bielefeld, Germany*
[3]*Omicron-Laserage Laserprodukte GmbH, Rodgau, Germany*
[4]*Excelitas PCO GmbH, Kelheim, Germany*
[5]*Department of General and Visceral Surgery, University Hospital OWL of the University of Bielefeld, Campus Bielefeld-Bethel, Bielefeld, Germany*
[6]*smsteinecker@physik.uni-bielefeld.de*
[7]*thomas.huser@physik.uni-bielefeld.de*

Abstract: Currently, super-resolution optical microscopy is mostly conducted with fluorophores that are excited and that emit in the visible part of the electromagnetic spectrum. Extending this range to the near-infrared (NIR) and even the shortwave-infrared (SWIR) part of the spectrum is highly desirable, because light in this wavelength range is less hazardous for live imaging and can penetrate much deeper into tissue. Here, we detail our development of a novel super-resolution structured illumination microscope that is purpose-built for imaging in the NIR wavelength range. Structured illumination via laser beam interference is accomplished by splitting the excitation light along two arms of a Michelson interferometer. Arbitrary illumination angles and a wide range of pattern spacings can be obtained by controlling a two-axis galvanometric mirror. Phase shifts of the pattern are accomplished by changing the angle of an anti-reflection-coated planoparallel glass plate inserted in one arm of the interferometer. Fluorescence is detected using a NIR-enhanced 26 Megapixel scientific Complementary Metal-Oxide-Semiconductor (sCMOS) camera. We characterize this system by imaging fluorescent beads with a diameter below the diffraction limit, and demonstrate its suitability for biological imaging by resolving cellular nanopores in the plasma membrane of liver sinusoidal endothelial cells.

1. Introduction

Imaging biological processes with a spatial resolution that exceeds the optical diffraction limit via super-resolution optical microscopy has seen exponential growth in recent years [1]. Multiple commercial implementations of various forms of super-resolution microscopy exist, e.g. stimulated emission depletion (STED) microscopy, single molecule localization microscopy (SMLM), or super-resolution structured illumination microscopy (SR-SIM). All of these implementations typically utilize the visible spectral wavelength range (approximately 400 – 700 nm) for imaging beyond the diffraction limit [1,2]. Imaging in this wavelength range is, however, hampered by absorption, scattering, photobleaching, and phototoxicity [3,4]. To overcome at least some of these issues, a number of fluorophores with increased photostability

#584208 https://doi.org/10.1364/OE.584208
Journal © 2026 Received 11 Nov 2025; revised 10 Dec 2025; accepted 10 Dec 2025; published 21 Jan 2026

Optics EXPRESS

have recently been developed, including organic fluorophores [5], fluorescent proteins [6], as well as inorganic fluorescent nanoparticles [7,8].

Scattering and absorption can be overcome by extending the wavelength range of optical microscopy to the near-infrared (NIR) and shortwave-infrared (SWIR) regions [9]. Fluorescence microscopy in the NIR and SWIR range is particularly desirable and has become a topic of intense research in recent years [10–12]. This development is complemented by the similarly rapid increase in research on detectors capable of detecting NIR and SWIR fluorescence with high quantum efficiency and high signal-to-noise ratio (SNR) [9,13]. Such detectors, especially single-photon counting quantum wires, are still very expensive and require liquid helium cooling [14,15]. NIR and SWIR image sensors, on the other hand, often display low SNR and limited pixel count [16]. These requirements have limited the extension of super-resolution microscopies to this wavelength range.

While SMLM and STED impose strict requirements for their successful implementation in the NIR spectral range – such as the need for NIR-emitting photo-switchable fluorophores, NIR-emitting fluorophores with high photostability, and the requirement for precise NIR laser beam shaping with spatial light modulators or phase masks [17,18] – SR-SIM is comparatively straightforward to implement. As long as the employed fluorophores are bright, stable, and exhibit a linear fluorescence response, SR-SIM can be readily extended to the NIR and SWIR spectral ranges [19–21]. Indeed, a few implementations of SR-SIM imaging in the NIR/SWIR region have already been demonstrated [21–24]. However, these typically either extend a system optimized for imaging in the VIS with an excitation source for NIR fluorescence, or they rely on digitally scanned laser beams to generate structured illumination [21,22]. The latter approach produces incoherent illumination patterns, resulting in reduced modulation contrast at high spatial frequencies and, consequently, a limited resolution gain [20,25].

Since the Abbe diffraction limit scales linearly with emission wavelength, spatial resolution in the NIR is intrinsically lower than in the visible range. This makes the application of SIM particularly advantageous in this spectral region, as it can partially compensate for the resolution loss due to longer wavelengths while retaining the inherent benefits of NIR imaging, such as reduced autofluorescence, deeper tissue penetration, and minimal phototoxicity [9,26].

Here, we detail our recent development of a SR-SIM system optimized for operation in the NIR spectral range. The microscope is based on a proprietary high-pixel-count NIR-enhanced sCMOS camera and uses fluorescence excitation at 785 nm. Interference patterns with a periodicity near the diffraction limit can be generated in the sample at arbitrary angles and phase steps via a Michelson-type interferometer optimized for operation with coherent excitation light in the NIR range. We characterize the system's performance using NIR-emitting fluorescent beads and demonstrate super-resolved NIR imaging by resolving nanopores in liver sinusoidal endothelial cells.

2. Materials and methods

Our implementation of a SR-SIM system dedicated to super-resolution imaging in the NIR spectral region is realized as a 2D structured illumination microscope centered around a Michelson-type interferometer. Schematics of the optical setup are shown in Fig. 1. A fiber-coupled 785 nm diode laser with a maximum power of 40 mW (BrixX 785-40NB, Omicron-Laserage Laserprodukte GmbH) is used as a NIR excitation source. The beam is collimated by a fiber collimator (RC04APC-P01, Thorlabs Inc.) and passed through an isolator (IO-5-NIR-LP, Thorlabs Inc.) to prevent back-reflections into the diode laser. A half-wave plate (HWP, WPH10M-808, Thorlabs Inc.) rotates the beam's polarization parallel to the optical table. This is important for polarization control of the setup, which is crucial for obtaining the highest modulation contrast in the SIM microscope [27].

Optics EXPRESS

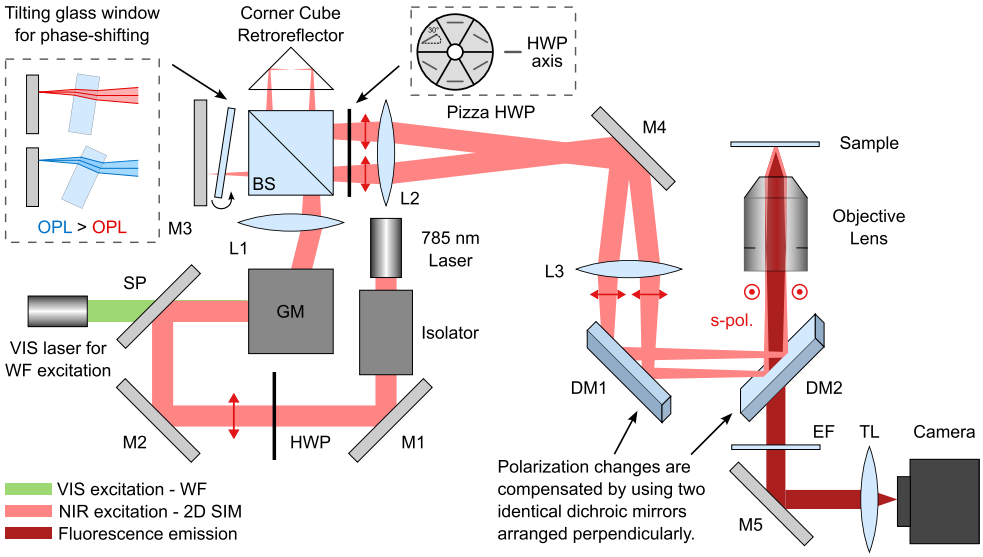

Fig. 1. Schematics of the NIR SIM setup. The 785 nm diode laser for NIR excitation is polarization-controlled and combined with a VIS laser for wide-field fluorescence excitation. SIM pattern generation is achieved by utilizing a Michelson-type interferometer, where a galvanometric mirror pair (GM) controls the pattern angle and periodicity and a custom phase modulator is used for phase shifting. A "pizza"-shaped half wave plate (HWP) ensures s-polarized excitation of the beam pairs in the sample plane. A beam pair is relayed and focused to the back focal plane (BFP) of the high-NA objective lens. Different pattern spacings can easily be generated by setting different angles of the GM and therefore adjusting the distance between the focal spots in the BFP of the objective lens. Fluorescence is collected via epi-detection, spectrally filtered and imaged onto the NIR enhanced sCMOS camera pco.edge 26 NIR.

The NIR beam is combined with a VIS beam (iChrome CLE-50, TOPTICA Photonics SE) for wide-field (WF) excitation using two silver-coated mirrors (M1 and M2, PF10-03-P01, Thorlabs Inc.) and a short-pass filter (SP, #69-206, Edmund Optics GmbH). The laser beam is then passed off-axis through a modified Michelson interferometer [28–30] by a pair of galvanometric mirrors (GM, dynAXIS 421, Scanlab GmbH). The scan mirrors are positioned at the back focal plane of a 150 mm achromatic doublet (L1, AC254-150-AB-ML, Thorlabs Inc.), which focuses the beam off-axis, but parallel to the optical axis through a 50/50 non-polarizing beamsplitter cube (BS, TWK 1.25, Bernhard Halle Nachfl. GmbH). The forward directed arm of the interferometer contains a hollow corner cube retroreflector (HRR201-P01, Thorlabs Inc.), which reflects and offsets the incident beam symmetrically to the optical axis. The other interferometer arm uses a silver-coated mirror (M3) to reflect the beam back onto itself. Mirror M3 is mounted on a micrometer stage (Spindler & Hoyer microcontrole) to match the path lengths of the interferometer arms. Furthermore, this interferometer arm contains a custom-built phase modulator for phase shifting. It is based on a modified galvanometer scanner (GVS001, Thorlabs Inc.), where the scan mirror was replaced by a NIR-coated glass window. Tilting the glass window changes the optical path length (OPL), generating different phases. Adding this element leads to a pure phase change and no displacement of the reflected beam, because the reflected beam travels through the plate on the exact same path. With precise calibration of the tilt angles, five distinct phases with equal phase steps are generated for the five phase images at each SIM angle. The angles and pattern spacing can be controlled by the galvanometric scan mirrors, providing high versatility. After their second pass through the beamsplitter cube, the two beams are combined to create an

Optics EXPRESS

opposing beam pair with an equal lateral offset from the optical axis. The linear polarization of each beam is rotated by a custom-built "pizza"-shaped half-wave plate with NIR-coating (Pizza HWP, AHWP6, Bolder Vision Optik Inc.). It consists of six wedge-shaped segments with axes oriented as shown in Fig. 1. This arrangement rotates the polarization of each beam pair to achieve s-polarized intersecting beams in the sample plane, ensuring maximum modulation depth [27]. A central hole of 1.5 mm diameter in the Pizza HWP is left open for homogeneous (non-patterned) wide-field illumination.

The beam foci are then relayed into the back focal plane (BFP) of the objective lens by a 4f-telescope (L2 and L3, AC508-300-AB-ML, Thorlabs Inc.) and two dichroic mirrors (DM1 and DM2, F68-785, AHF Analysetechnik AG). Currently, no off-the-shelf polarization-maintaining dichroic mirrors are available that cover typical VIS wavelengths as well as the NIR wavelength used here. To compensate for polarization changes introduced by the coating of standard dielectric mirrors, two dichroic mirrors from the same batch are oriented orthogonally (horizontal and vertical) in the beam path [31]. A PlanApo 60× 1.45 NA TIRF oil-immersion objective lens from Olympus is used to create the interference pattern of the two beams in the sample plane of a custom-built inverted microscope. Piezo-actuated XYZ sample stages (Q-545.240, Physik Instrumente (PI) SE & Co. KG) hold and position the sample relative to the objective lens. The fluorescence signal is collected via epi-detection by the same objective lens, filtered by emission filters (EF, F40-784 and F76-748, AHF Analysetechnik AG), reflected by mirror M5, and focused onto the sCMOS camera by a 180 mm tube lens (U-SWATLU, Olympus). Images are recorded using a proprietary NIR-enhanced camera with 26.2 megapixels (pco.edge 26 NIR, Excelitas PCO GmbH).

Currently, the setup provides a field of view (FOV) of approximately 60 µm in diameter in the sample plane, covering only part of the camera sensor. This limitation was chosen deliberately to maintain a higher power density in the sample plane given the restricted output power of the employed diode laser. The projected pixel size is 41.6 nm in the image plane, resulting in a pixel size of 20.8 nm of the reconstructed SR-SIM image. A custom PCB board with a Teensy 4.1 microcontroller (PJRC) is used to control the setup and to coordinate the movement of the scan mirrors, phase modulator, and camera triggering via a custom-written Python script. The Python script offers a graphical user interface where the user can set the pattern spacing, phase modulator voltages, and move the setup to specific angles and phases for alignment. The remaining part of the laser beams that passes through the second dichroic mirror is used to monitor the back focal plane positions (BFP) of the beams with an industrial CMOS camera (UI-3060CP-M-GL Rev. 2, IDS Imaging Development Systems GmbH, not shown) positioned in the same distance as the BFP of the objective lens. The three-axis sample stage has a repeatability of 6 nm, allowing for z-stack image acquisitions with an adjustable step size. Image data are acquired and displayed using MicroManager [32].

Image reconstruction is accomplished with the Fiji plugin fairSIM [33] which uses the Gustafsson super-resolution SIM reconstruction method [34]. In this work, 15 SIM images (3 angles and 5 phase images each) are recorded and used for image reconstruction. fairSIM provides the reconstructed super-resolution SIM image, a pseudo-wide-field image (Pseudo-WF), which is generated by averaging all 15 raw images into one image, and a Wiener-filtered pseudo-wide-field image (Filtered WF).

2.1. Characterization of the pco.edge 26 NIR camera

Our SR-SIM setup uses a NIR-enhanced high-pixel-count sCMOS camera, the pco.edge 26 NIR. This camera utilizes a NIR-enhanced sCMOS image sensor, which provides a significantly improved quantum efficiency in the near-infrared spectral region, as can be seen in Fig. 2(c). The quantum efficiency of the regular pco.edge 26 is shown in blue, and the quantum efficiency of the pco.edge 26 NIR is shown in red. In the range between approximately 700 nm – 900 nm, the

Optics EXPRESS

pco.edge 26 NIR should provide roughly double the signal of the pco.edge 26. In order to test the performance of this camera for super-resolution microscopy in the NIR region, we prepared a sample containing 100 nm fluorescent beads (TetraSpeck Microspheres, 0.1 μm, fluorescent, ThermoFisher). The sample was excited at 639 nm using a previously reported fiberSIM setup [35]. Raw SIM images were collected and split 50:50 with an image-splitter and then sent to a pco.edge 26 and pco.edge 26 NIR, respectively. The resulting reconstructed SR-SIM images of the bead sample are shown in Fig. 2(a) and Fig. 2(b). Note that both images are shown with the same intensity scale and contain the same FOV of the bead sample. For better visibility, the FOVs shown in Fig. 2 were selected from a much larger FOV. As can be seen from these images, as well as the cross sections shown in Fig. 2(d), the signal provided by the pco.edge 26 NIR is almost double that of the pco.edge 26.

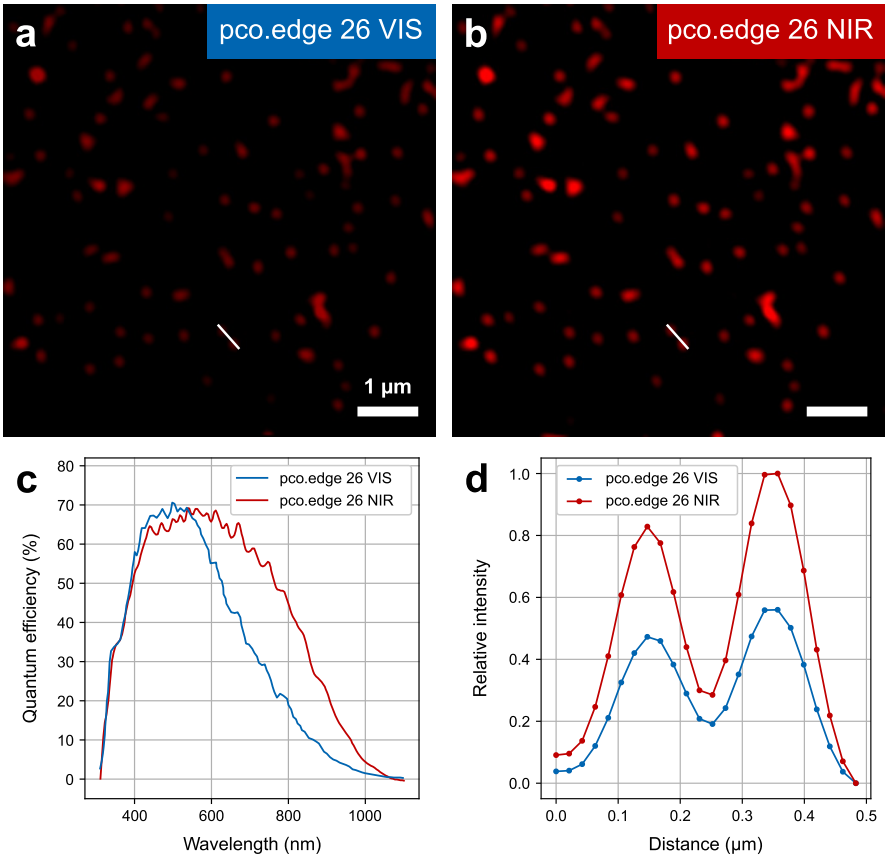

Fig. 2. FairSIM-reconstructed SIM images of 100 nm Tetraspeck fluorescent beads excited at 639 nm. The SIM raw images were recorded with a pco.edge 26 VIS (a) and pco.edge 26 NIR (b). Images are displayed on the same intensity scale, showing higher bead brightness with the pco.edge 26 NIR. (c) Quantum efficiency curves highlight the improved sensitivity of the NIR-enhanced camera above ~550 nm. (d) Line profiles through two beads from (a) and (b) confirm close to doubled signal intensity and improved signal-to-noise ratio with the pco.edge 26 NIR.

2.2. *Sample preparation*

To test the imaging performance of our NIR-enhanced SR-SIM, two types of samples were prepared.

Optics EXPRESS

For the first sample, #1.5 coverslips were coated with poly-L-lysine for 10 min, rinsed, and incubated with 200 nm NIR-fluorescent beads (Near-IR Fluorescent Degradex PLGA, Phosphorex LLC). After air-drying, the coverslips were mounted in a 1:1 mixture of glycerol and double-distilled water on microscope slides and sealed with nail polish.

For the second sample, liver sinusoidal endothelial cells (LSECs) were isolated from RjHan:NMRI mice at the Animal Facility of Bielefeld University. The isolation protocol was described in detail previously [36]. Immediately after sacrificing the animal, the liver was perfused, enzymatically digested and the cells were separated using different centrifugation steps. The LSECs were isolated from the non-parenchymal cell fraction in a final step using CD-146 coated magnetic beads (MACS, Miltenyi).

A total of 2.5×10^6 cells/ml were seeded in EGM medium containing 2% FBS on #1.5 borosilicate glass coverslips coated with 0.2 mg/ml fibronectin. The coverslips were stored in an incubator at 37°C with 5% CO_2 and 5% O_2 until the cells were used for the experiment.

The membrane of the cells was stained with a 1:1000 dilution of BioTracker NIR790 Cytoplasmic Membrane Dye (SCT115, Merck KGaA) in CO_2-independent medium (Gibco, ThermoFisher) for 20 min at 37°C. After staining, the cells were rinsed three times with fresh CO_2-independent medium and fixed with 3% glyoxal in PBS for 30 min at room temperature [37]. Before imaging, the cells were washed three times with PBS and mounted in a reducing and oxidizing agent buffer system (ROXS) consisting of ascorbic acid as reducing and methylviologen as oxidizing agent to minimize photobleaching [38]. Samples were sealed with nail polish.

3. Results and discussion

3.1. Evaluating SR-SIM imaging performance in the NIR

A sample consisting of fluorescent beads with a diameter below the optical diffraction limit is well suited for determining the resolution improvement obtained by our NIR implementation of a SR-SIM system. For reference, the Abbe diffraction limit for 820 nm fluorescence emission with the objective lens used in our system is approximately 283 nm. Depending on the bead concentration in the solution, the sample can form islands of bead clusters, as well as isolated single or few-bead clusters on the coverslip surface. The NIR-enhanced sCMOS camera enables the acquisition of 2D raw images with high signal-to-noise ratio in the near-infrared region, from which the super-resolved SR-SIM image is reconstructed. To test our system's imaging performance we chose a sample composed of 200 nm NIR-fluorescent beads (see Fig. 3). The Pseudo-wide-field image of a 21.3 μm × 21.3 μm field of view is shown in Fig. 3(a). Underneath the Pseudo-WF image, an enlarged image of the region of interest (indicated by a white outline in the Pseudo-WF image) is shown. As is apparent from these images and the cross section shown in Fig. 3(d), the Pseudo-WF image cannot resolve two 200 nm beads lying directly next to each other. The Filtered WF images shown in Fig. 3(b) result in a moderate resolution gain, allowing for the separation of clusters of beads that cannot be clearly separated in the Pseudo-WF images. However, only the SR-SIM reconstructed images provide the resolution gain required to clearly distinguish neighboring beads, as shown in Fig. 3(c). This is further accentuated by the cross sections shown in Fig. 3(d), where only the line profile obtained from the SR-SIM image clearly shows two adjacent beads which are indistinguishable in cross sections of the WF images. The center-to-center distance of these beads was determined to be 228 nm by fitting a two-peak Gaussian function to the SIM line profile. We found the NIR-emitting beads to exhibit significant signal variations in their fluorescence, which explains the significant differences in visibility of the beads in all of the fluorescence images.

Optics EXPRESS

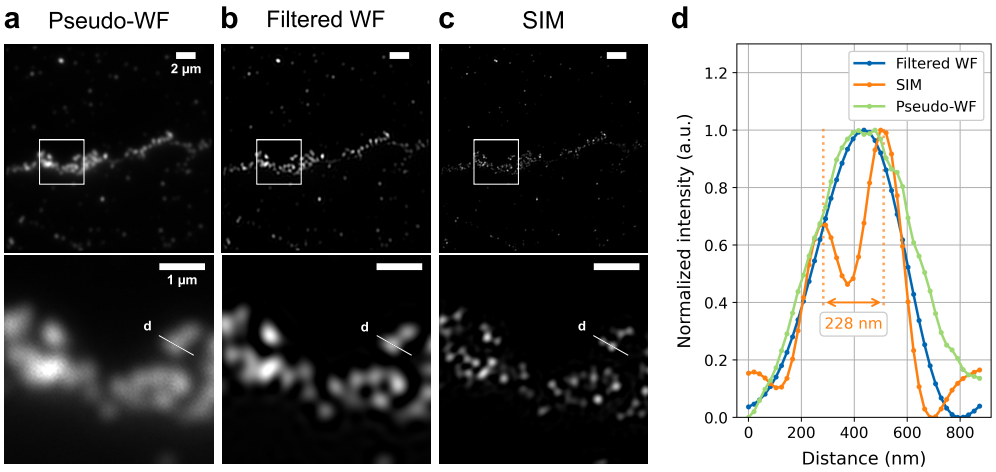

Fig. 3. Imaging of 200 nm NIR fluorescent beads in a 21.3 µm × 21.3 µm FOV. Resolution enhancement is evident when comparing the Pseudo-WF (a) and Filtered WF (b) images with the SR-SIM reconstruction (c). Enlarged regions (4.5 µm × 4.5 µm) highlight that SIM resolves single beads that are indistinguishable in the Pseudo-WF or Filtered WF images. A line profile through two beads (d) further confirms this: while the beads cannot be separated in Pseudo-WF or Filtered WF, they are clearly resolved in the SIM image. Fitting a two-peak Gaussian function to the SIM line profile indicated a center-to-center bead distance of 228 nm. Exposure time: 50 ms per single raw SR-SIM image.

3.2. Quantitative analysis of the system's spatial resolution in the NIR

To further quantify the resolution enhancement obtained by SR-SIM in the NIR, we conducted a Fourier Ring Correlation (FRC) analysis on the images obtained from the NIR-fluorescent bead sample (see Fig. 4) [39]. The FRC curve for the WF image initially showed unrealistically high correlations that could not have been transmitted through the optical system. Investigation of the camera sensor revealed that these spurious correlations originated from fixed-pattern noise, thus components that emerge after the microscope's pass-band, and that are not part of the desired signal to be analyzed by FRC. This effect of CMOS pattern noise is known and consistent with previous reports [40].

To correct for this, the FRC threshold criteria need to be modified and dynamically adapted to compensate for correlated noise contributions [40]. This is achieved by replacing the original fixed threshold of $\frac{1}{7}$ with a threshold that is dynamically derived by fitting the horizontal plateau (containing information components physically beyond the instruments pass-band), and then determining the spatial resolution from the intersection of the linear drop-off of the signal correlation with the fitted noise floor. For visual representation, data is shown both in raw form and normalized to a common noise floor. While this modification needs to be taken into account when comparing with other FRC results using the fixed $\frac{1}{7}$ threshold, this method allows to apply FRC on a wide range of area detectors like CMOS sensors, which tend to add fixed pattern noise to their signals.

This analysis yielded a spatial resolution of 321 nm for the WF image (Fig. 4(a)), which is slightly above the expected Abbe limit of 283 nm for 820 nm fluorescence emission. This deviation can be attributed to residual system misalignment as well as the use of 200 nm beads, because the recorded bead profile represents the convolution of bead size and the system's point spread function (PSF). 100 nm fluorescent beads would provide a closer approximation to point emitters and yield FRC-derived resolutions closer to the theoretical diffraction limit, but at the time of this writing we were unable to find a commercial source for NIR-fluorescent 100 nm

Optics EXPRESS

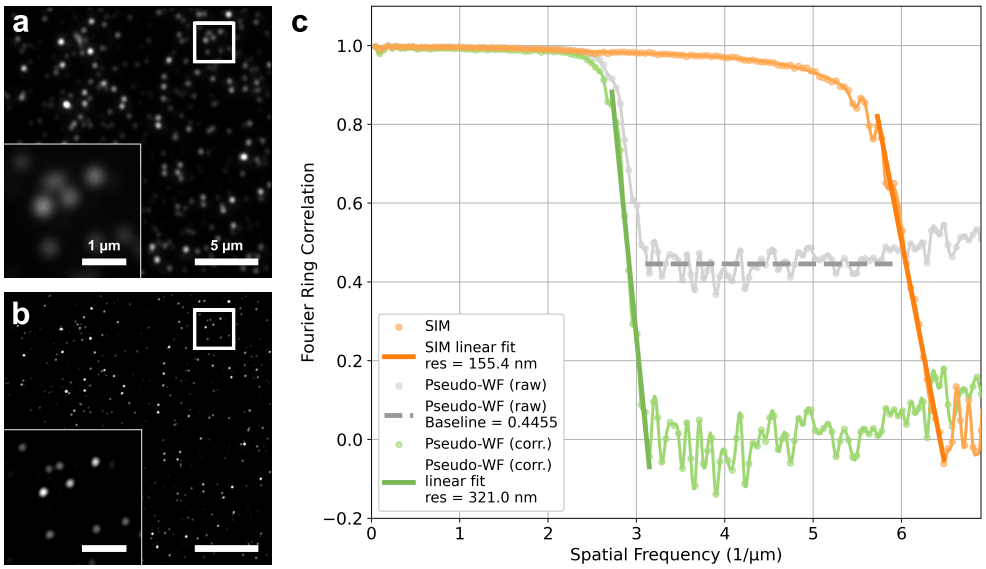

Fig. 4. An FRC analysis was performed at a different position of the same bead sample as used before for the Pseudo-WF image (a) and the corresponding SIM reconstruction (b). To correct for fixed-pattern signal from the camera, which caused unrealistically high correlations in the raw FRC curve (grey), the horizontal plateau was fitted and subtracted (green). From the intersection of the fitted linear drop-off with the noise floor (see FRC section in results), we obtained resolutions of 321.0 nm (Pseudo-WF) and 155.4 nm (SIM), indicating a 2.07-fold resolution enhancement. Exposure time: 80 ms per single raw SR-SIM image.

beads. For the SIM image (Fig. 4(b)), the FRC analysis yielded a spatial resolution of 155 nm, corresponding to a 2.07-fold resolution improvement.

3.3. *Imaging nanopores in fluorescently stained primary endothelial cells*

Next, we evaluated the imaging performance of our NIR SR-SIM system for biomedical applications by imaging subcellular nanopores in primary murine liver sinusoidal endothelial cells (LSEC). These nanopores in mouse LSEC, called fenestrations, have a typical diameter of 80 – 200 nm and support the primary filter function of the liver by allowing small particles dissolved in the blood, such as lipoproteins and small molecules, to pass from the blood into the liver [41,42]. These cells form a single layer on the inside of the liver's vasculature. LSEC from young, healthy donors can have up to several thousands of such nanopores that cover up to 60% of their surface. Fenestrae are grouped in sieve plates, which contain up to several 10s of nanopores and are isolated by filaments of the cytoskeletal protein F-actin [43]. The ability to image the number, size and dynamics of fenestrae is important because these parameters partially reflect the functional state and health of the liver, including its filtration efficiency and response to physiological or pathological stimuli [42]. However, these features are largely beyond the resolving power of conventional optical microscopes, requiring the use of super-resolution techniques. Currently, there are no known surface markers that allow for the specific fluorescent staining of fenestrae. Instead, the entire plasma membrane of LSECs has to be labeled [44]. This creates a negative imaging contrast, since fenestrae appear as unstained holes, which is challenging for most super-resolution techniques. SIM, however, can still resolve these structures effectively, as the structured illumination pattern enhances spatial frequency information and improves the visualization of small unstained areas. Imaging living LSEC with fluorescent dyes

Optics EXPRESS

and illumination with visible light leads to the creation of reactive oxygen species, which cause rapid apoptosis of the cells [4,45]. Thus, using NIR-fluorescent membrane dyes and excitation in the deep red or NIR should be beneficial, as this wavelength range is less phototoxic to cells and also provides much deeper penetration depths in 3D cell cultures and tissues due to reduced absorption and scattering. Before we can use this strategy in live imaging, however, we need to determine the imaging performance and spatial resolution that can be obtained by this approach. Figure 5 shows fairSIM reconstructions of a fixed LSEC stained with BioTracker NIR790. Dark holes in the plasma membrane are only partially visible or indistinct in the Pseudo-WF (Fig. 5(a)) and Filtered WF (Fig. 5(b)) images, but are clearly resolved in the SIM reconstruction (Fig. 5(c)). Magnified regions highlight that unstained areas in the Filtered WF image blur together, whereas the SIM image reveals fine membrane structures that subdivide these areas into smaller nanopores reminiscent of fenestrae. This shows that SR-SIM is necessary to accurately investigate the fenestration size and distribution.

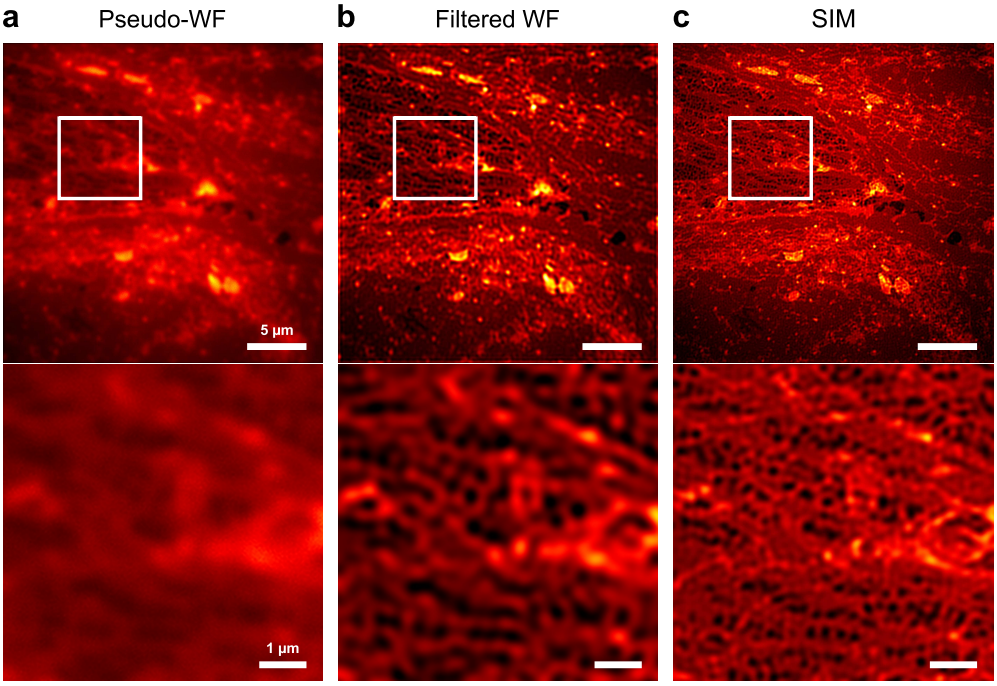

Fig. 5. Fluorescence images of fixed LSECs, whose plasma membrane is stained with BioTracker NIR790. The first row shows a FOV of 26.7 µm × 26.7 µm. The Pseudo-WF image (a) shows the lowest resolution. In the Filtered WF image (b), additional membrane details become visible, but they are most clearly defined in the SIM reconstruction (c). The second row shows magnified regions (~6.5 µm × 6.5 µm) that further emphasize the resolution improvement. While nanopores appear indistinct in the Pseudo-WF image and only larger unstained areas are visible in the Filtered WF image, the SIM reconstruction resolves these regions into smaller, individual nanopores reminiscent of fenestrae. Exposure time: 10 ms per single raw SR-SIM image.

The average fluorescence intensity in the raw data sets fluctuates up to 15.6% when using the ROXS buffer described in Section 2.2. We found that in the absence of the ROXS buffer, the fluorescent signal decayed rapidly, making it impossible to acquire 15 SIM images with good SNR. This underlines the importance of incorporating a reducing and oxidizing agent buffer

Optics EXPRESS

system when imaging with the BioTracker NIR790 dye (and probably also other NIR dyes), as photobleaching and the formation of long-lived triplet states is minimized.

4. Conclusions

In summary, we have developed a novel implementation of a structured illumination microscope dedicated to super-resolution fluorescence imaging in the near-infrared region. The system is centered around a Michelson-type interferometer and provides great flexibility in the pattern angles and pattern spacing that can be achieved to excite fluorescence in the sample. In addition, the microscope is inherently fast – its speed is only limited by the galvanometric mirrors, laser power, and camera readout – and inherently achromatic, except for optical coatings and filters. Previous publications that have extended SR-SIM to imaging in the NIR spectral range either used a SIM microscope optimized for imaging in the visual part of the optical spectrum and combined it with a NIR excitation source [22], or they extended the spatial resolution via striped or multifocal illumination [21,24]. In comparison, we presented a dedicated SR-SIM system capable of imaging in the NIR spectral range with a greater than 2x improved spatial resolution, which only a coherent SR-SIM system generating interference patterns with diffraction-limited periodicity can achieve and with enhanced detection sensitivity well into the NIR range. We have characterized the imaging performance of this system by imaging 200 nm NIR-fluorescent beads. We have independently determined the spatial resolution that can be achieved with this system to be 155.4 nm at an excitation wavelength of 785 nm based on Fourier Ring Correlation. This corresponds to a 2.07-fold resolution improvement over the Abbe limit. We have also demonstrated the use of this system for imaging biological samples by resolving nanopores in the plasma membrane of liver sinusoidal endothelial cells. Currently the field of view of this microscope is limited by the laser power of the narrow-band diode laser and by the photophysics of NIR-fluorescent dyes. Both these limitations can be solved, however, opening up a wide range of applications in NIR-fluorescence-based super-resolution biomedical imaging.

Funding. Universitätsbibliothek Bielefeld (Open Access Publication Fund); Bundesministerium für Bildung und Forschung (13N15827, 13N15830); HORIZON EUROPE European Innovation Council (Pathfinder Open, grant agreement no. 101046928); Deutsche Forschungsgemeinschaft (540217954).

Acknowledgment. This project was supported by the German Federal Ministry for Research, Technology and Aeronautics (BMFTR), through project BetterView (FKZ 13N15827, 13N15830). This work also received funding from the European Union's European Innovation Council PATHFINDER Open Programme under grant agreement No 101046928. T.H. and J. S.a.E. further acknowledge funding by the Deutsche Forschungsgemeinschaft (DFG, German Science Foundation), project number 540217954.

Disclosures. Gerhard Holst is an employee of Excelitas PCO GmbH, the manufacturer of the proprietary pco.edge 26 NIR-enhanced sCMOS camera utilized in this work. Sönke Baumann is an employee of Omicron-Laserage Laserprodukte GmbH, the manufacturer of the 785 nm fiber-coupled diode laser used in this work. All other authors have no conflicts to disclose.

Data availability. The data underlying the results presented in this paper are not publicly available at this time but may be obtained from the authors upon reasonable request.

References

1. L. Schermelleh, A. Ferrand, T. Huser, *et al.*, "Super-resolution microscopy demystified," Nat. Cell Biol. **21**(1), 72–84 (2019).
2. L. Mezache and C. Leterrier, "Advancing super-resolution microscopy: Recent innovations in commercial instruments," Microsc. Microanal. **31**(2), ozaf004 (2025).
3. M. A. Reiche, J. S. Aaron, U. Boehm, *et al.*, "When light meets biology – how the specimen affects quantitative microscopy," J. Cell Sci. **135**(6), jcs259656 (2022).
4. J. Icha, M. Weber, J. C. Waters, *et al.*, "Phototoxicity in live fluorescence microscopy, and how to avoid it," BioEssays **39**(8), 1700003 (2017).
5. D.-H. Kim, H. M. Triet, S. H. Lee, *et al.*, "Super-photostable organic dye for long-term live-cell single-protein imaging," Nat. Methods **22**(3), 550–558 (2025).
6. M. Hirano, R. Ando, S. Shimozono, *et al.*, "A highly photostable and bright green fluorescent protein," Nat. Biotechnol. **40**(7), 1132–1142 (2022).

Optics EXPRESS

7. C. Lee, E. Z. Xu, K. W. C. Kwock, *et al.*, "Indefinite and bidirectional near-infrared nanocrystal photoswitching," Nature **618**(7967), 951–958 (2023).
8. F. Ren, F. Wang, A. Baghdasaryan, *et al.*, "Shortwave-infrared-light-emitting probes for the in vivo tracking of cancer vaccines and the elicited immune responses," Nat. Biomed. Eng. **8**(6), 726–739 (2023).
9. O. T. Bruns, T. S. Bischof, D. K. Harris, *et al.*, "Next-generation in vivo optical imaging with short-wave infrared quantum dots," Nat. Biomed. Eng. **1**(4), 0056 (2017).
10. J. A. Carr, D. Franke, J. R. Caram, *et al.*, "Shortwave infrared fluorescence imaging with the clinically approved near-infrared dye indocyanine green," Proc. Natl. Acad. Sci. **115**(17), 4465–4470 (2018).
11. E. D. Cosco, A. L. Spearman, S. Ramakrishnan, *et al.*, "Shortwave infrared polymethine fluorophores matched to excitation lasers enable non-invasive, multicolour in vivo imaging in real time," Nat. Chem. **12**(12), 1123–1130 (2020).
12. F. Wang, Y. Zhong, O. Bruns, *et al.*, "In vivo NIR-II fluorescence imaging for biology and medicine," Nat. Photonics **18**(6), 535–547 (2024).
13. B. Zhu and H. Jonathan, "A review of image sensors used in near-infrared and shortwave infrared fluorescence imaging," Sensors **24**(11), 3539 (2024).
14. R. E. Correa, E. A. Dauler, G. Nair, *et al.*, "Single Photon Counting from Individual Nanocrystals in the Infrared," Nano Lett. **12**(6), 2953–2958 (2012).
15. I. Charaev, D. A. Bandurin, A. T. Bollinger, *et al.*, "Single-photon detection using high-temperature superconductors," Nat. Nanotechnol. **18**(4), 343–349 (2023).
16. D. Roblyer, A. Pilvar, T. Pham, *et al.*, "Review of shortwave infrared imaging and spectroscopy in tissue [invited]," Biomed. Opt. Express **16**(12), 5028–5062 (2025).
17. Z.-H. Wu, X. Zhu, Q. Yang, *et al.*, "Near-Infrared Perylenecarboximide Fluorophores for Live-Cell Super-Resolution Imaging," J. Am. Chem. Soc. **146**(11), 7135–7139 (2024).
18. M. Kamper, H. Ta, N. A. Jensen, *et al.*, "Near-infrared STED nanoscopy with an engineered bacterial phytochrome," Nat. Commun. **9**(1), 4762 (2018).
19. Y. Wu and H. Shroff, "Faster, sharper, and deeper: Structured illumination microscopy for biological imaging," Nat. Methods **15**(12), 1011–1019 (2018).
20. R. Heintzmann and T. Huser, "Super-Resolution Structured Illumination Microscopy," Chem. Rev. **117**(23), 13890–13908 (2017).
21. F. Wang, Z. Ma, Y. Zhong, *et al.*, "In vivo NIR-II structured-illumination light-sheet microscopy," Proc. Natl. Acad. Sci. **118**(6), e2023888118 (2021).
22. X. Lu, X. Zhuang, Y. Dong, *et al.*, "Super-Photostability and Super-Brightness of EC5 Dyes for Super-Resolution Microscopy in the Deep Near-Infrared Spectral Region," Chem. Mater. **36**(2), 949–958 (2024).
23. B. Liu, C. Chen, X. Di, *et al.*, "Upconversion nonlinear structured illumination microscopy," Nano Lett. **20**(7), 4775–4781 (2020).
24. L. Feng, S. Cai, J. Zhang, *et al.*, "Nir-ii multifocal structured illumination microscopy," Opt. Lett. **47**(18), 4656–4659 (2022).
25. J. D. Manton, "Answering some questions about structured illumination microscopy," Philos. Trans. Royal Soc. A: Math. Phys. Eng. Sci. **380**(2220), 20210109 (2022).
26. J. A. Carr, M. Aellen, D. Franke, *et al.*, "Absorption by water increases fluorescence image contrast of biological tissue in the shortwave infrared," Proc. Natl. Acad. Sci. **115**(37), 9080–9085 (2018).
27. K. O'Holleran and M. Shaw, "Polarization effects on contrast in structured illumination microscopy," Opt. Lett. **37**(22), 4603–4605 (2012).
28. R. Marchand, H. Ortkrass, D. Aziz, *et al.*, "Super-resolution live-cell fluorescence lifetime imaging," arXiv (2025).
29. J. Roth, J. Mehl, and A. Rohrbach, "Fast tirf-sim imaging of dynamic, low-fluorescent biological samples," Biomed. Opt. Express **11**(7), 4008–4026 (2020).
30. M. Brunstein, K. Wicker, K. Hérault, *et al.*, "Full-field dual-color 100-nm super-resolution imaging reveals organization and dynamics of mitochondrial and er networks," Opt. Express **21**(22), 26162–26173 (2013).
31. M. Lachetta, G. Wiebusch, W. Hübner, *et al.*, "Dual color dmd-sim by temperature-controlled laser wavelength matching," Opt. Express **29**(24), 39696–39708 (2021).
32. A. Edelstein, N. Amodaj, K. Hoover, *et al.*, "Computer control of microscopes using μmanager," Curr. Protoc. Mol. Biol. **92**(1), 14.20.1 (2010).
33. M. Müller, V. Mönkemöller, S. Hennig, *et al.*, "Open-source image reconstruction of super-resolution structured illumination microscopy data in ImageJ," Nat. Commun. **7**(1), 10980 (2016).
34. M. G. L. Gustafsson, "Surpassing the lateral resolution limit by a factor of two using structured illumination microscopy," J. Microsc. **198**(2), 82–87 (2000).
35. H. Ortkrass, J. Schürstedt, G. Wiebusch, *et al.*, "High-speed tirf and 2d super-resolution structured illumination microscopy with a large field of view based on fiber optic components," Opt. Express **31**(18), 29156–29165 (2023).
36. K. Elvevold, I. Kyrrestad, and B. Smedsrød, "Protocol for isolation and culture of mouse hepatocytes (hcs), kupffer cells (kcs), and liver sinusoidal endothelial cells (lsecs) in analyses of hepatic drug distribution," in *Antisense RNA design, delivery, and analysis*, (Springer US New York, NY, 2022), pp. 385–402.
37. K. N. Richter, N. H. Revelo, K. J. Seitz, *et al.*, "Glyoxal as an alternative fixative to formaldehyde in immunostaining and super-resolution microscopy," The EMBO J. **37**(1), 139–159 (2018).

Optics EXPRESS

38. J. Vogelsang, R. Kasper, C. Steinhauer, *et al.*, "A reducing and oxidizing system minimizes photobleaching and blinking of fluorescent dyes," Angewandte Chemie Int. Ed. **47**(29), 5465–5469 (2008).
39. R. P. J. Nieuwenhuizen, K. A. Lidke, M. Bates, *et al.*, "Measuring image resolution in optical nanoscopy," Nat. Methods **10**(6), 557–562 (2013).
40. R. Van den Eynde, A. Sandmeyer, W. Vandenberg, *et al.*, "Quantitative comparison of camera technologies for cost-effective super-resolution optical fluctuation imaging (sofi)," J. Phys: Photonics **1**(4), 044001 (2019).
41. K. K. Sørensen, J. Simon-Santamaria, R. S. McCuskey, *et al.*, "Liver Sinusoidal Endothelial Cells," Compr. Physiol. **5**(4), 1751–1774 (2015).
42. C. I. Øie, V. Mönkemöller, W. Hübner, *et al.*, "New ways of looking at very small holes – using optical nanoscopy to visualize liver sinusoidal endothelial cell fenestrations," Nanophotonics **7**(3), 575–596 (2018).
43. V. Mönkemöller, C. Øie, W. Hübner, *et al.*, "Multimodal super-resolution optical microscopy visualizes the close connection between membrane and the cytoskeleton in liver sinusoidal endothelial cell fenestrations," Sci. Rep. **5**(1), 16279 (2015).
44. V. C. Cogger, G. P. McNerney, T. Nyunt, *et al.*, "Three-dimensional structured illumination microscopy of liver sinusoidal endothelial cell fenestrations," J. Struct. Biol. **171**(3), 382–388 (2010).
45. R. Dixit and R. Cyr, "Cell damage and reactive oxygen species production induced by fluorescence microscopy: effect on mitosis and guidelines for non-invasive fluorescence microscopy," The Plant J. **36**(2), 280–290 (2003).